

Three-dimensional passive seismic waveform imaging around the SAFOD site, California, using the generalized Radon transform

Haijiang Zhang,¹ Ping Wang,¹ Robert D. van der Hilst,¹ M. Nafi Toksoz,¹ Clifford Thurber,² and Lupei Zhu³

Received 11 August 2009; revised 30 October 2009; accepted 10 November 2009; published 9 December 2009.

[1] We apply a three-dimensional (3D) generalized Radon transform (GRT) to scattered P-waves from 575 local earthquakes recorded at 68 temporary network stations for passive-source imaging of (near-vertical) structures close to the San Andreas Fault Observatory at Depth (SAFOD) site. The GRT image profiles through or close by the SAFOD site reveal near-vertical reflectors close to the fault zone as well as in the granite to the southwest and the Franciscan mélange to the northeast of the main fault. Although slightly lower in resolution, these structures are generally similar to features in 2D images produced with steep-dip prestack seismic migration of data from active source seismic reflection and refraction surveys. Our GRT images, however, also reveal several vertical reflectors to the northeast of the SAF that do not appear in the migration images but which are consistent with local geology. These results suggest that in a seismically active area, inverse scattering of earthquake data (for instance with the GRT) can be a viable and, in 3D, economic alternative to an active source survey. **Citation:** Zhang, H., P. Wang, R. D. van der Hilst, M. N. Toksoz, C. Thurber, and L. Zhu (2009), Three-dimensional passive seismic waveform imaging around the SAFOD site, California, using the generalized Radon transform, *Geophys. Res. Lett.*, 36, L23308, doi:10.1029/2009GL040372.

1. Introduction

[2] As one of the projects of the EarthScope initiative, the San Andreas Fault Observatory at Depth (SAFOD) involves drilling into a seismogenic section of the San Andreas fault (SAF) in order to study fundamental issues regarding earthquakes and fault mechanics [Hickman *et al.*, 2004]. To image at kilometer-scale the three dimensional (3D) structure of the region around the drill site and to provide well-constrained locations for drilling into targeted earthquake zones, a temporary seismic array, known as PASO (Parkfield Area Seismic Observatory), was installed around Parkfield (CA) in 2000 [Thurber *et al.*, 2003] (Figure 1c). Seismic tomography with PASO data showed a strong velocity contrast across the SAF, faster to the southwest and slower to the northeast [e.g., Thurber *et al.*, 2003; Zhang *et al.*, 2009] (Figure 1d). This velocity contrast reflects differ-

ences in elastic properties of geological terrains on either side of the SAF, with the Salinian block southwest of the fault and Franciscan mélange (uncomfortably overlain by unmetamorphosed sedimentary rocks of the Great Valley sequence) to the northeast (Figures 1a and 1b).

[3] Seismic tomography can, however, only resolve the smooth variations in elastic properties in Earth's interior. To image structure at length scales smaller than what can be resolved tomographically, including elasticity contrasts across faults, one must use the scattered seismic wavefield (for instance, reflections and phase conversions). Inverse scattering has been used to characterize the detailed fault zone structure near the SAFOD site using controlled source data. For example, Kirchhoff prestack depth migration has been applied to data from a ~5 km long seismic reflection/refraction survey known as PSINE, shot in 1998 [Catchings *et al.*, 2002], to image an active SAF trace to a depth of ~1 km [Hole *et al.*, 2001, 2006]. Kirchhoff migration of a much longer seismic reflection/refraction line across the SAFOD site (shot in 2003) detected several near-vertical reflectors to a depth of 5 km on both sides of the SAF [Bleibinhaus *et al.*, 2007]. In addition to these active-source experiments, Kirchhoff migration of scattered waves from microearthquakes recorded at borehole sensors in the SAFOD pilot hole detected the SAF at depth, as well as four secondary faults [Chavarria *et al.*, 2003].

[4] Here, we explore the feasibility of using a generalized Radon transform (GRT) for the passive imaging of near-vertical faults in the shallow part of the crust around the SAFOD site. We use waveform data from 575 microearthquakes recorded at 68 PASO and HRSN network stations (Figure 1c) and we evaluate the success of passive source GRT imaging through comparison with results of controlled source depth migration [Bleibinhaus *et al.*, 2007].

2. Methodology

[5] The GRT is an inverse scattering method that has been extensively used in exploration seismology [Beylkin, 1985; Miller *et al.*, 1987]. Only recently the method has begun to be applied to passive seismic (that is, earthquake) data for the imaging of Earth's structure at greater depths [e.g., Bostock and Rondenay, 1999; Rondenay *et al.*, 2005; Chambers and Woodhouse, 2006; Wang *et al.*, 2006, 2008; van der Hilst *et al.*, 2007].

[6] Assuming single scattering, the medium parameters (stiffness tensor, density) can be decomposed into smooth variations, c_0 , which can be inferred from seismic tomography, and a (non-smooth) perturbation, δc , which contains the discontinuities and other types of scatterers, and which can be estimated with inverse scattering (e.g., GRT). Like-

¹Earth Resources Laboratory, Department of Earth, Atmospheric, and Planetary Sciences, Massachusetts Institute of Technology, Cambridge, Massachusetts, USA.

²Department of Geoscience, University of Wisconsin-Madison, Madison, Wisconsin, USA.

³Department of Earth and Atmospheric Sciences, Saint Louis University, Saint Louis, Missouri, USA.

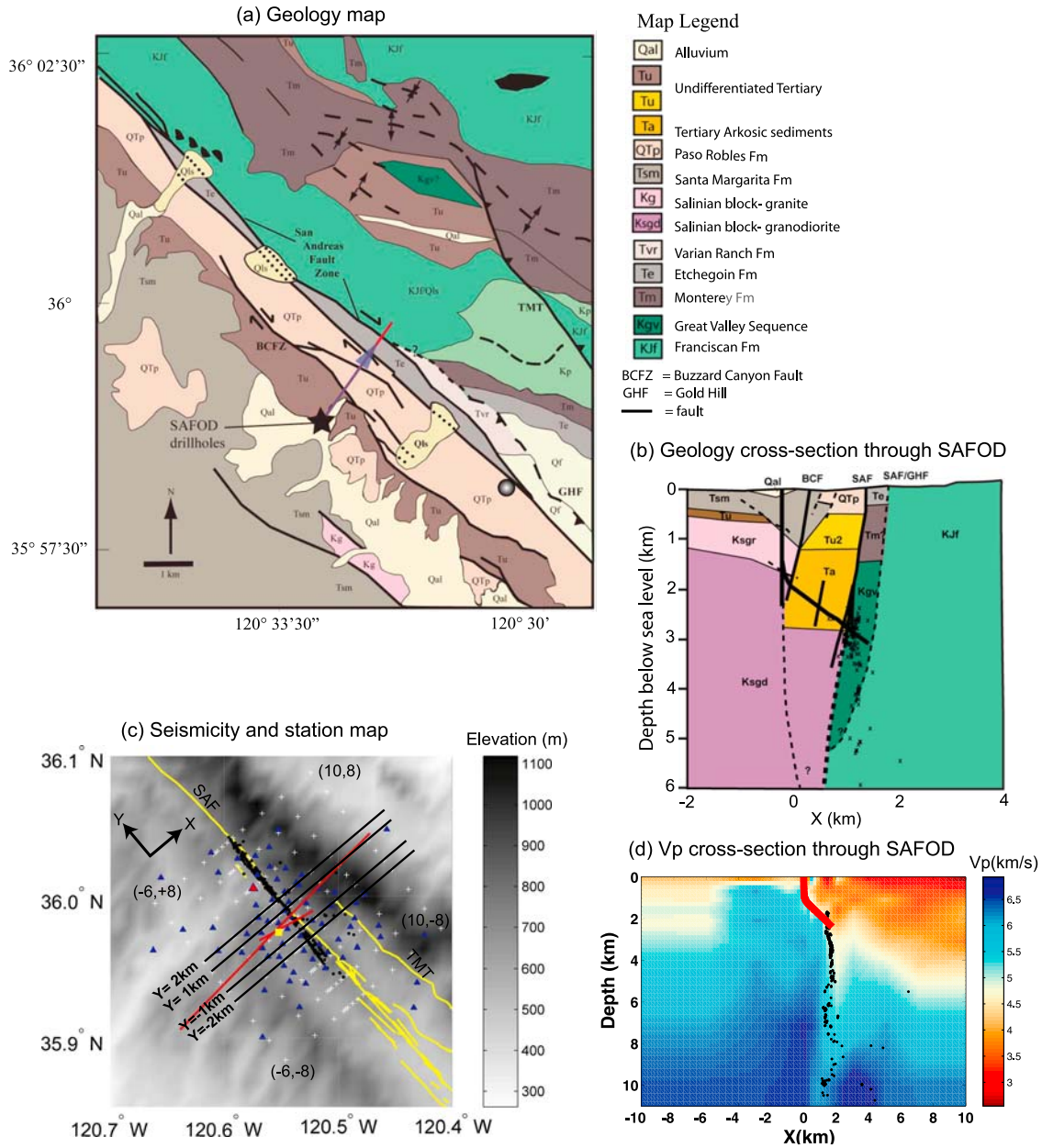


Figure 1. (a) Geological map of the area around the SAFOD site (modified from *Bradbury et al.* [2007]). (b) Across-fault cross section of the geology model through the SAFOD site (modified from *Bradbury et al.* [2007]). (c) Map of seismicity (black dots), seismic stations (blue triangles), and faults (yellow lines) around SAFOD (yellow square). The coordinate center is located at the SAFOD site with Y axis directs positive northwest and X axis directs positive northeast. The background is the topography elevation. Shorter and longer red lines through SAFOD indicate the active seismic reflection/refraction surveys in 1998 and 2003. (d) Across fault cross section of the Vp model through SAFOD.

wise, the wavefield u can be decomposed into the part u_0 that is associated with wave propagation in c_0 and δu , which is the scattered wavefield due to δc . Figure 2 (bottom) illustrates the scattering geometry around SAFOD that is used for our approach. Consider a wave from a source at \mathbf{x}^s to a receiver at \mathbf{x}^r that is scattered at \mathbf{y} ; signal arriving at a particular time in a single record can be produced by scattering at points \mathbf{y} anywhere along an isochron (but not all parts of the isochron contribute equally to the recorded signal, see below). The slowness vector of the ray connecting \mathbf{x}^s with \mathbf{y} (at \mathbf{y}) is given by $\mathbf{p}^s(\mathbf{y})$ and $\mathbf{p}^r(\mathbf{y})$ denotes the

slowness vector of the ray from \mathbf{x}^r to \mathbf{y} . The migration slowness vector, which controls image resolution, is then given by $\mathbf{p}^m(\mathbf{y}) = \mathbf{p}^s(\mathbf{y}) + \mathbf{p}^r(\mathbf{y})$. Furthermore, θ is the scattering angle between $\mathbf{p}^s(\mathbf{y})$ and $\mathbf{p}^r(\mathbf{y})$ and ψ is the azimuth (with respect to north) of the plane through \mathbf{x}^s , \mathbf{x}^r , and \mathbf{y} .

[7] For specific combinations of scattering angle θ and azimuth ψ , the GRT maps seismograph network data to an image of the target location \mathbf{y} (Figure 2), and different combinations of θ and azimuth ψ yield different images of the same structure. These multiple images in the angle

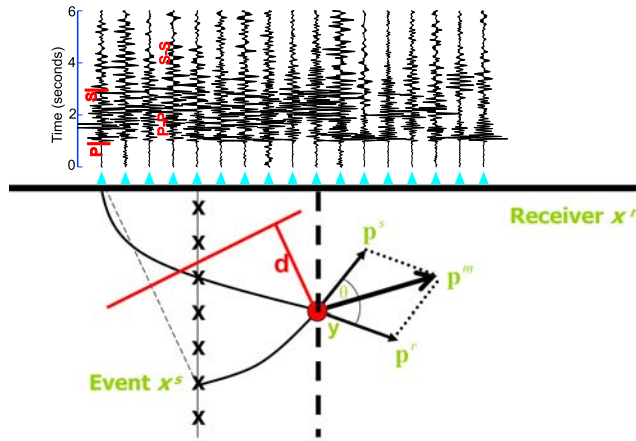


Figure 2. (bottom) Geometry at the scattering point for earthquakes (crosses) and receivers (triangles) around SAFOD. θ is the scattering angle between the slowness vectors $\mathbf{p}^s(\mathbf{y})$ and $\mathbf{p}^r(\mathbf{y})$. \mathbf{p}^m is the migration slowness vector and \mathbf{y} is the image point. d is the distance from the image point \mathbf{y} to the middle plane between the source and the receiver. (top) An example of recordings at different stations from an earthquake located at depth about 3 km.

domain, also known as common image-point gathers $I(\mathbf{y}; \theta, \psi)$, or IGs, represent the data redundancy that allows inverse scattering to resolve structures at spatial scales smaller than the Fresnel zones of the associated waves. After Wang *et al.* [2006] we write

$$I(\mathbf{y}; \theta, \psi) = \int W(\mathbf{x}^s, \mathbf{x}^r, \mathbf{y}) \tilde{u}^{(1)}(\mathbf{x}^s, \mathbf{x}^r, \mathbf{y}) |\mathbf{p}^m(\mathbf{y})|^3 dV^m, \quad (1)$$

where $\tilde{u}^{(1)}(\mathbf{x}^s, \mathbf{x}^r, \mathbf{y})$ represents the singly scattered waveform data transformed to $\mathbf{x}^s, \mathbf{x}^r, \mathbf{y}$ space, $W(\mathbf{x}^s, \mathbf{x}^r, \mathbf{y})$ is a taper window, and $\mathbf{p}^m(\mathbf{y})$ the migration slowness vector defined above. $W(\mathbf{x}^s, \mathbf{x}^r, \mathbf{y})$ restricts the structural sensitivity of the data to the part of the isochron (which can be viewed as the sensitivity kernel of the imaging operator) in the neighborhood of the specular reflection. The taper window $W(\mathbf{x}^s, \mathbf{x}^r, \mathbf{y})$ is defined by

$$W(\mathbf{x}^s, \mathbf{x}^r, \mathbf{y}) = \begin{cases} 0 & \text{when } d > D \\ \cos(d/D) & \text{when } d \leq D \end{cases}, \quad (2)$$

where D is a pre-selected distance that is related to the frequency bands and structure scales ($D = 1$ km in this study) and d is the distance from the image point \mathbf{y} to the middle plane between the source and the receiver (Figure 2). We note that equation (1) is different from the formulation used by Wang *et al.* [2006] in that the simple taper replaces the weights associated with source radiation. The radiation effect is similar for all events, because most micro-earthquakes around SAFOD have the same focal mechanism (strike-slip on vertical planes) [Thurber *et al.*, 2006], and, therefore, not accounted for in this application.

[8] The common image-point gathers $I(\mathbf{y}; \theta, \psi)$ reveal multi-scale variations in elastic properties. Any (local) reflector should show up at (or close to) the same position

for each processed angle θ and ψ provided an adequate 3D background velocity c_0 . However, we integrate over scattering azimuth ψ , that is, $I(\mathbf{y}; \theta, \psi) \rightarrow I(\mathbf{y}; \theta)$, in order to enhance signal to noise in view of uneven angle coverage and data noise. Finally, a structural image at \mathbf{y} is obtained through integrating over scattering angle θ , that is, $I(\mathbf{y}; \theta) \rightarrow I(\mathbf{y})$.

[9] To obtain the weight factor $|\mathbf{p}^m(\mathbf{y})|$ we first calculate travel times for each source, image, and receiver point (using a finite-difference scheme – see below) and then calculate the travel time gradients at image points \mathbf{y} : for the wave from the source this gives $\nabla T^s(\mathbf{y}) = \mathbf{p}^s(\mathbf{y})$ and for the receiver leg $\nabla T^r(\mathbf{y}) = \mathbf{p}^r(\mathbf{y})$. The magnitude of the migration slowness vector is then

$$|\mathbf{p}^m(\mathbf{y})| = |\mathbf{p}^s(\mathbf{y}) + \mathbf{p}^r(\mathbf{y})| = \frac{2}{v(\mathbf{y})} \cos\left(\frac{1}{2} \arccos\left(\frac{\mathbf{p}^s(\mathbf{y}) \cdot \mathbf{p}^r(\mathbf{y})}{|\mathbf{p}^s(\mathbf{y})| \cdot |\mathbf{p}^r(\mathbf{y})|}\right)\right), \quad (3)$$

where $v(\mathbf{y})$ is the velocity value at the image point \mathbf{y} .

3. Data

[10] We collected seismic waveforms from 575 earthquakes recorded by 61 PASO and 7 HRSN stations for the period of 2001 to 2002. Figure 2 (top) shows an example of recordings at different stations from an earthquake located at depth about 3 km. The direct P and S wave arrivals and the P-to-P and S-to-S scattered (coda) waves are clearly visible. In this study we apply the GRT only to the vertical component P-P scattered waves, and data processing involves several steps. To reduce contamination from converted S wave energy we mute the waveform segment starting from the first S arrival; S-P scattering may contribute to the late coda of the P-arrival, but its effect on the GRT images is expected to be small because S-P waves have different move-outs and will be suppressed by stacking over P-P slowness. The highest effective frequency content of the seismic waveforms recorded by PASO network (at a sampling rate 0.01 s) is around 15 Hz, so we used a 1.5–15 Hz pass band to filter the data. With $V_p \sim 5$ –6 km/s near SAFOD, the smallest P-wave wavelength is then ~ 300 –400 m, which is close to the smallest scale resolved in our recent V_p model [Zhang *et al.*, 2009]. Subsequently, the P-P waveforms are normalized with respect to the amplitude of the direct P wave. Finally, to prevent annihilation of data with opposite polarities, before stacking we check and align polarities using predictions from strike-slip faulting, the common focal mechanism of Parkfield earthquakes [Thurber *et al.*, 2006].

[11] We parameterized the image volume around SAFOD using a three-dimensional grid of imaging (or scattering) points \mathbf{y} with a spacing of 200 m in all three directions. For each of these grid nodes, a travel-time table is calculated – using a finite-difference scheme [Podvin and Lecomte, 1991] – for all source and receiver locations using the earthquake locations and the 3D V_p model due to Zhang *et al.* [2009]. Upon imaging, the travel time for a particular source-scatterer-receiver (that is, \mathbf{x}^s - \mathbf{y} - \mathbf{x}^r) path is calculated from these tables. The corresponding scattered seismic waveform amplitude is taken as an average of 5 samples before and after the calculated scattered P arrival time

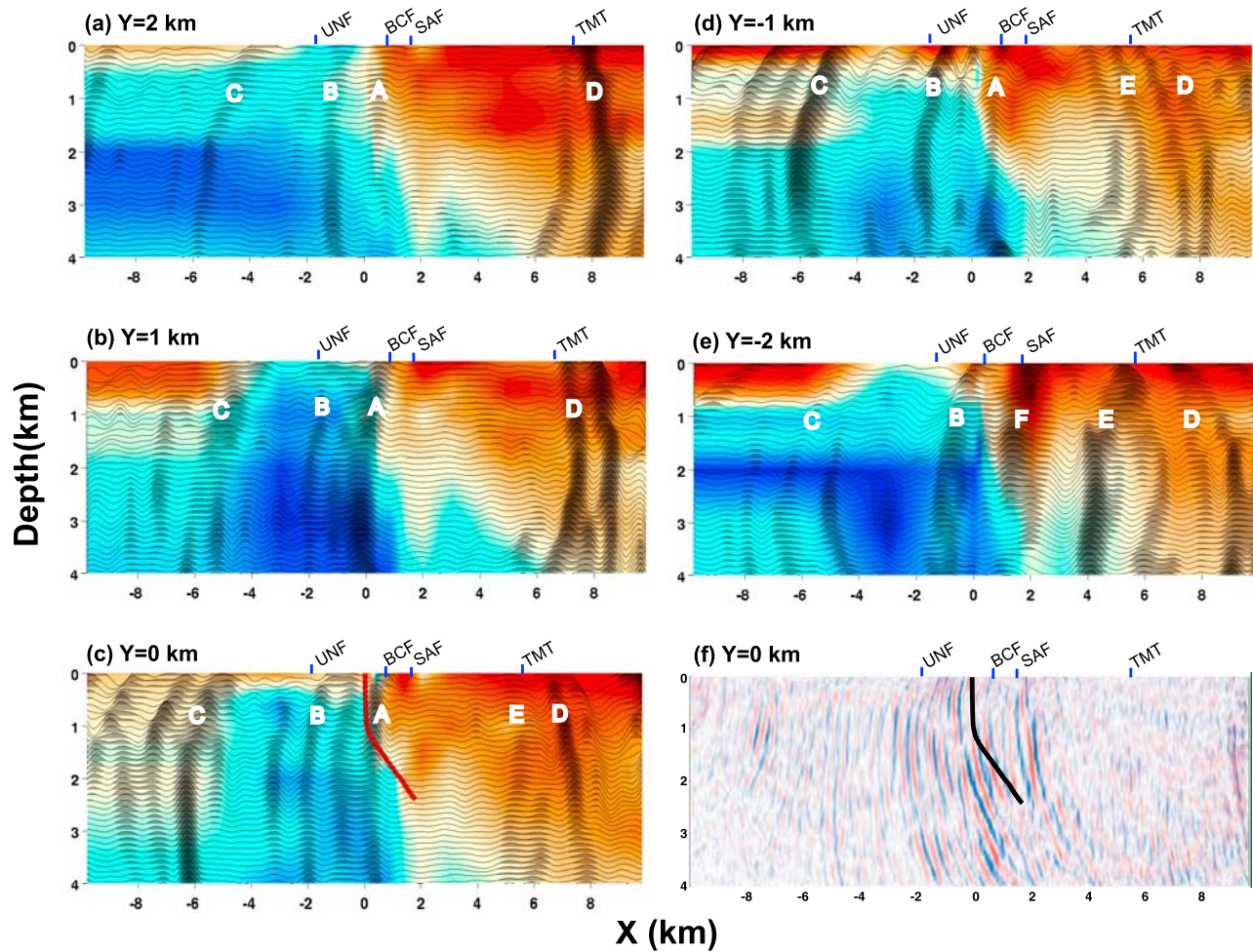


Figure 3. Cross sections of the P-P scattering images at (a) $Y = 2$, (b) $Y = 1$, (c) $Y = 0$, (d) $Y = -1$, and (e) $Y = -2$ km. Red thick line on the section $Y = 0$ km is the SAFOD borehole profile. The background is the V_p image with the color bar shown in Figure 1d. (f) The seismic migration image using active sources by *Bleibinhaus et al.* [2007] for comparison. Note that the plotting method of scattering image emphasizes the vertical structures. BCF, Buzzard Canyon Fault; UNF, Un-Named Fault; TMT, Table Mountain Thrust; SAF, San Andreas Fault.

(to account for the velocity model uncertainty). According to equation (1), the corresponding P-P scattered waveform segment is then weighted by taper $W(\mathbf{x}^s, \mathbf{x}^r, \mathbf{y})$ and migration slowness vector $|\mathbf{p}^m(\mathbf{y})|$, calculated according to equation (3). As confirmed by tests with synthetic data (see auxiliary material), we do not have to remove the direct P wave segments because they have little effect on the final GRT images due to the use of the weight factor $|\mathbf{p}^m(\mathbf{y})|$.¹ This allows the imaging of scatter zones (albeit at lower resolution) near the seismic sources; without weighting such signals would need to be muted because they have travel times close to those of the direct waves.

4. Results

[12] Tests with synthetic data computed for the same seismic source and station geometry as in the inversion of observed data indicate that GRT imaging can resolve structure within 3 km from SAFOD site (measured along

strike of SAF), that is, $Y = -3$ to 3 km, and to a depth of 4 km (see auxiliary material; note that the SAFOD site is at $X = 0$ km, $Y = 0$ km). Artifacts (including “smearing”) may appear because of the limitations of source and receiver geometry, but their amplitudes are small compared to the structures discussed here. Figure 3 shows the cross-sections of P-P scattering images at $Y = 2, 1, 0, -1$ and -2 km. For comparison, it also displays a result of steep-dip prestack depth migration from a controlled source reflection/refraction survey [*Bleibinhaus et al.*, 2007].

[13] The GRT images reveal a strong reflector (A) near $X = 0$ km at a location near the surface trace of the Buzzard Canyon Fault (BCF) [*Bradbury et al.*, 2007], and a series of near-vertical seismic reflectors are imaged on both sides of the seismic source region near $X = 1.7$ km (i.e., the SAF). There are also strong reflectors within the Salinian granite to the southwest of the SAF, similar to those found by *Bleibinhaus et al.* [2007]. Reflector B (at $X \sim -2$ km) coincides with a fault that separates the Santa Margarita Formation to the west from intact granodiorites to the east [*Bradbury et al.*, 2007; *Zhang et al.*, 2009]. The weaker vertical structures that show up around reflector B may

¹Auxiliary materials are available in the HTML. doi:10.1029/2009GL040372.

correspond to multiple intrusive cycles in the granite, as suggested by *Bleibinhaus et al.* [2007]. Such heterogeneity is also supported by tomographically inferred variations in propagation speed (Figure 1d) and by variations in magnetic susceptibility variations observed in the SAFOD pilot hole [*McPhee et al.*, 2004]. In addition, a group of relatively strong reflectors (denoted by C) is detected southwest of $X = -6$ km.

[14] A series of vertical structures appears to the northeast of the SAF, but they generally have lower amplitudes than those to the southwest and we cannot rule out that they are smearing artifacts. However, a strong reflector (D) is located at $X = 8$ km, some 1–2 km northeast of the Table Mountain Thrust (TMT, Figures 1a and 3) identified by *Bradbury et al.* [2007]. The Waltham Canyon Fault detected by *Bleibinhaus et al.* [2007] is on the edge of our model area and is not imaged very well. Both to the northwest ($Y = 1$ and 2) and southeast ($Y = 0, -1, -2$) of the SAFOD site several reflectors (including E) exist between reflectors A and D.

5. Discussion and Concluding Remarks

[15] The structures detected by GRT imaging with (micro)earthquake data are generally in good agreement with the results of pre-stack depth migration of data from a controlled-source reflection and refraction survey [*Bleibinhaus et al.*, 2007]. The GRT images have lower spatial resolution, however, because the seismic waveforms used in passive seismic imaging have lower frequency content than data in controlled-source imaging. The effective frequency is further reduced (to about 5 Hz) by the 11-sample averaging of waveform data used to account for velocity model uncertainty.

[16] In contrast to the active-source migration of *Bleibinhaus et al.* [2007] our GRT does not resolve structure related to the SAF and Gold Hill Fault (GHF). This can be explained with the relationship between GRT image resolution and scatter angle [*Wang et al.*, 2006]: near-source scattering is often associated with large scattering angles, which yield low image resolution (see Auxiliary Material). However, the strong, broad reflector F, at $X \sim 2$ km on section $Y = -2$ km (Figure 3) may correspond to the SAF. To the southeast of SAFOD, the Parkfield earthquakes start to shift southwestward from the main SAF trace and instead follow the Southwest Fracture Zone (Figure 1c). This allows imaging the SAF, albeit with somewhat lower resolution than with controlled (active) source surveys.

[17] The group of reflectors (C) observed to the southwest of $X = -6$ km is located near the edge of the well resolved part of the 3D velocity model [*Zhang et al.*, 2009]. Their locations may thus be biased, but they also appear in the migration image of *Bleibinhaus et al.* [2007] and are likely to be real. This structure may represent the steep sediment-granite contact.

[18] The image sections at $Y = -1$ and -2 km reveal more structure between reflectors A and D than sections further north. This difference is consistent with the local geology: southwest of $Y = -1$ km a complex sequence of rock units is exposed east of the SAF whereas further north a relatively uniform Franciscan formation is located east of the SAF (Figure 1a). The imaged reflectors may not all

indicate faults, but it is likely that they represent lateral contrasts in elasticity at depth. We note that these structures do not appear in the active source migration profiles (Figure 3).

[19] In this study, the variations in dip angle of the reflectors in the GRT images are likely to be an artifact of the limited source-receiver distribution. Because of incomplete sampling of the subsurface, isochrones (that is, the impulse response of the imaging operator) for seismic sources and receivers around SAFOD can leave an imprint on the images. Indeed, clustering of seismic sources along a plane, as in this study, may be the worst case scenario for the GRT imaging; interpretation of changes in dip angle of seismic reflectors will be more meaningful in regions where the seismic sources are distributed more evenly and over a broader region.

[20] To study the shallow sub-surface near the SAFOD site with data from the PASO and HRSN arrays we adapted the generalized Radon transform as developed for the characterization of the core-mantle boundary with ScS and SKKS waves recorded at global networks [*Wang et al.*, 2006, 2008; *van der Hilst et al.*, 2007]. From the encouraging agreement with results from active source migration and with known geological features we conclude that GRT with passive seismic source data is indeed able to detect faults and other elasticity contrasts on a local scale, provided that data from dense arrays is available. The source-receiver geometry exploited here is not ideal for GRT imaging, but as denser receiver arrays are being deployed around the world, such as the USArray component of EarthScope [*Meltzer et al.*, 1999], passive seismic imaging with methods such as the GRT used here could become routine practice for the mapping and characterization of fault zones.

[21] **Acknowledgments.** The work presented here was supported by the Department of Energy under grant DE-FG3608GO18190 (HZ and MNT), the National Science Foundation under grants EAR-0346105 and EAR-0454511 (CT), EAR-0609969 (LZ) and EAR-0757871 (RvdH), and MIT's Earth Resources Laboratory (PW). Constructive reviews by John Hole and Florian Bleibinhaus helped us improve the paper. We thank NSF for the continued support of EarthScope as well as the many people who work every day to make it as successful as it is.

References

- Beylkin, G. (1985), Imaging of discontinuities in the inverse scattering problem by inversion of a causal generalized Radon transform, *J. Math. Phys.*, 26, 99–108, doi:10.1063/1.526755.
- Bleibinhaus, F., J. A. Hole, T. Ryberg, and G. S. Fuis (2007), Structure of the California coast ranges and San Andreas fault at SAFOD from seismic waveform inversion and reflection imaging, *J. Geophys. Res.*, 112, B06315, doi:10.1029/2006JB004611.
- Bostock, M. G., and S. Rondenay (1999), Migration of scattered teleseismic body waves, *Geophys. J. Int.*, 137, 732–746, doi:10.1046/j.1365-246x.1999.00813.x.
- Bradbury, K. K., D. C. Barton, J. G. Solum, S. D. Draper, and J. P. Evans (2007), Mineralogic and textural analyses of drill cuttings from the San Andreas Fault Observatory at Depth (SAFOD) boreholes: Initial interpretations of fault zone composition and constraints on geologic models, *Geosphere*, 3, 299–318, doi:10.1130/GES00076.1.
- Catchings, R. D., M. J. Rymer, M. R. Goldman, J. A. Hole, R. Huggins, and C. Lippus (2002), High-resolution seismic velocities and shallow structure of the San Andreas Fault Zone at Middle Mountain, Parkfield, California, *Bull. Seismol. Soc. Am.*, 92, 2493–2503, doi:10.1785/0120010263.
- Chambers, K., and J. H. Woodhouse (2006), Investigating the lowermost mantle using migrations of long-period S-ScS data, *Geophys. J. Int.*, 166, 667–678, doi:10.1111/j.1365-246X.2006.03002.x.
- Chavarria, J. A., P. Malin, R. D. Catchings, and E. Shalev (2003), A look inside the San Andreas fault at Parkfield through vertical seismic profiling, *Science*, 302, 1746–1748, doi:10.1126/science.1090711.

- Hickman, S., M. Zoback, and W. Ellsworth (2004), Introduction to special section: Preparing for the San Andreas Fault Observatory at Depth, *Geophys. Res. Lett.*, **31**, L12S01, doi:10.1029/2004GL020688.
- Hole, J. A., R. D. Catchings, K. C. St Clair, M. J. Rymer, D. A. Okaya, and B. J. Carney (2001), Steep-dip seismic imaging of the shallow San Andreas Fault near Parkfield, *Science*, **294**, 1513–1515, doi:10.1126/science.1065100.
- Hole, J. A., T. Ryberg, G. Fuis, F. Bleibinhaus, and A. Sharma (2006), Structure of the San Andreas fault zone at SAFOD from a seismic refraction survey, *Geophys. Res. Lett.*, **33**, L07312, doi:10.1029/2005GL025194.
- McPhee, D., R. Jachens, and C. Wentworth (2004), Crustal structure across the San Andreas Fault at the SAFOD site from potential field and geologic studies, *Geophys. Res. Lett.*, **31**, L12S03, doi:10.1029/2003GL019363.
- Meltzer, A., et al. (1999), The USArray Initiative (USArray Steering Committee), *GSA Today*, **9**, 8–10.
- Miller, D. E., M. Oristaglio, and G. Beylkin (1987), A new slant on seismic imaging: Migration and integral geometry, *Geophysics*, **52**, 943–964, doi:10.1190/1.1442364.
- Podvin, P., and I. Lecomte (1991), Finite difference computation of travel-time in very contrasted velocity model: A massively parallel approach and its associated tools, *Geophys. J. Int.*, **105**, 271–284, doi:10.1111/j.1365-246X.1991.tb03461.x.
- Rondenay, S., M. G. Bostock, and K. M. Fischer (2005), Multichannel inversion of scattered teleseismic body waves: Practical considerations and applicability, in *Seismic Earth: Array Analysis of Broadband Seismograms*, *Geophys. Monogr. Ser.*, vol. 157, edited by A. Levander and G. Nolet, pp. 187–203, AGU, Washington, D. C.
- Thurber, C., S. Roecker, K. Roberts, M. Gold, L. Powell, and K. Rittger (2003), Earthquake locations and three-dimensional fault zone structure along the creeping section of the San Andreas fault near Parkfield, CA: Preparing for SAFOD, *Geophys. Res. Lett.*, **30**(3), 1112, doi:10.1029/2002GL016004.
- Thurber, C., H. Zhang, F. Waldhauser, J. Hardebeck, A. Michael, and D. Eberhart-Phillips (2006), Three-dimensional compressional wave-speed model, earthquake relocations, and focal mechanisms for the Parkfield, California, region, *Bull. Seismol. Soc. Am.*, **96**, S38–S49, doi:10.1785/0120050825.
- van der Hilst, R. D., M. V. de Hoop, P. Wang, S.-H. Shim, P. Ma, and L. Tenorio (2007), Seismo-stratigraphy and thermal structure of Earth's core-mantle boundary region, *Science*, **315**, 1813–1817, doi:10.1126/science.1137867.
- Wang, P., M. V. de Hoop, R. D. van der Hilst, P. Ma, and L. Tenorio (2006), Imaging of structure at and near the core mantle boundary using a generalized Radon transform: 1. Construction of image gathers, *J. Geophys. Res.*, **111**, B12304, doi:10.1029/2005JB004241.
- Wang, P., M. V. De Hoop, and R. D. van der Hilst (2008), Imaging of the lowermost mantle (D'') and the core-mantle boundary with SKKS coda waves, *Geophys. J. Int.*, **175**, 103–115, doi:10.1111/j.1365-246X.2008.03861.x.
- Zhang, H., C. Thurber, and P. Bedrosian (2009), Joint inversion for V_p , V_s , and V_p/V_s at SAFOD, Parkfield, California, *Geochem. Geophys. Geosyst.*, **10**, Q11002, doi:10.1029/2009GC002709.
- C. Thurber, Department of Geoscience, University of Wisconsin-Madison, 1215 West Dayton St., Madison, WI 53706, USA.
- M. N. Toksoz, R. D. van der Hilst, P. Wang, and H. Zhang, Earth Resources Laboratory, Department of Earth, Atmospheric, and Planetary Sciences, Massachusetts Institute of Technology, 77 Massachusetts Ave., Cambridge, MA 02139, USA. (hjzhang@mit.edu)
- L. Zhu, Department of Earth and Atmospheric Sciences, Saint Louis University, 3507 Laclede Ave., Saint Louis, MO 63108, USA.